Neutron spin echo shows pHLIP is capable of retarding membrane thickness fluctuations

Haden L. Scott, Violeta Burns-Casamayor, Andrew C. Dixson, Robert F. Standaert, Christopher B. Stanley, Laura-Roxana Stingaciu, Jan-Michael Y. Carrillo, Bobby G. Sumpter, John Katsaras, Wei Qiang, Frederick A. Heberle, Blake Mertz, Rana Ashkar, Francisco N. Barrera

PII: S0005-2736(24)00080-4

DOI: https://doi.org/10.1016/j.bbamem.2024.184349

Reference: BBAMEM 184349

To appear in: *BBA - Biomembranes*

Received date: 21 January 2024

Revised date: 3 April 2024

Accepted date: 21 May 2024

Please cite this article as: H.L. Scott, V. Burns-Casamayor, A.C. Dixson, et al., Neutron spin echo shows pHLIP is capable of retarding membrane thickness fluctuations, *BBA - Biomembranes* (2023), https://doi.org/10.1016/j.bbamem.2024.184349

NEUTRON SPIN ECHO SHOWS pHLIP IS CAPABLE OF RETARDING MEMBRANE THICKNESS FLUCTUATIONS

Haden L. Scott,[a] Violeta Burns-Casamayor,[b] Andrew C. Dixson,[a] Robert F. Standaert,[a,b,c] Christopher B. Stanley,[d,e] Laura-Roxana Stingaciu,[f,g] Jan-Michael Y. Carrillo,[e,h] Bobby G. Sumpter,[e,h] John Katsaras,[d,f,i] Wei Qiang,[j] Frederick A. Heberle,[k] Blake Mertz,[b,l] Rana Ashkar* [m,n] and Francisco N. Barrera* [a]

[a] Department of Biochemistry & Cellular and Molecular Biology, University of Tennessee, Knoxville 37996

[b] C. Eugene Bennett Department of Chemistry, West Virginia University, Morgantown, WV 26506

[c] Biosciences Division, Oak Ridge National Laboratory, Oak Ridge, TN 37831

[d] Shull Wollan Center – a Joint Institute for Neutron Sciences, Oak Ridge, TN 37831

[e] Computational Sciences and Engineering Division, Oak Ridge National Laboratory, Oak Ridge, TN 37831

[f] Labs and Soft Matter Group, Neutron Scattering Division, Oak Ridge National Laboratory, Oak Ridge, TN 37831

[g] JCNS1, FZJ outstation at SNS, Oak Ridge National Laboratory, Oak Ridge, TN 37831

[h] Center for Nanophase Materials Sciences, Oak Ridge, TN 37831

[i] Department of Physics and Astronomy, University of Tennessee, Knoxville, TN 37996

[j] Department of Chemistry, the State University of New York, Binghamton, NY 13902

[k] Department of Chemistry, University of Tennessee, Knoxville, TN 37920

[l] West Virginia University Cancer Institute, Morgantown, WV 26506

[m] Department of Physics, Virginia Tech, Blacksburg, VA 24061

[n] Center for Soft Matter and Biological Physics, Virginia Tech, Blacksburg, VA 24061

Correspondence: ashkar@vt.edu; fbarrera@utk.edu

Abstract: Cell membranes are responsible for a range of biological processes that require interactions between lipids and proteins. While the effects of lipids on proteins are becoming better understood, our knowledge of how protein conformational changes influence membrane dynamics remains rudimentary. Here, we performed experiments and computer simulations to study the dynamic response of a lipid membrane to changes in the conformational state of pH-low insertion peptide (pHLIP), which transitions from a surface-associated (SA) state at neutral pH to a transmembrane (TM) α-helix under acidic conditions. Our results show that TM-pHLIP significantly slows down membrane thickness fluctuations due to an increase in effective membrane viscosity. Our findings suggest a possible membrane regulatory mechanism, where the TM helix affects lipid tail conformations, and subsequently alters membrane fluctuations and viscosity.

Keywords. Lipid-protein interactions, MD simulations, membrane viscosity, membrane dynamics.

Introduction

Cell membranes perform and regulate key biological functions through a delicate interplay between lipids and proteins (1-5). Examples range from the role of membrane curvature during the photochemical cycle of rhodopsin and the gating behavior of mechanosensitive channels (6-8), to the regulatory effect of membrane thickness on the enzymatic activity of membrane proteins (3, 9, 10). Overall, these studies have significantly contributed to our understanding of how the structural features of lipid membranes, such as bilayer thickness and curvature, can influence the function of membrane-associated proteins (11-13). Despite these advances, major gaps still exist in our understanding of how membrane proteins alter the properties of their host membranes. More importantly, while it is accepted that membranes play a key role in the spatiotemporal regulation of protein-lipid interactions, for example, in cell signaling (14-16), our knowledge of membrane dynamics is still in its nascent stages (17). Conformational molecular changes and collective motions prompted by environmental cues or molecular recognition (18-20) are not only central to biological function, but can significantly inform the next generation biosensors, therapeutics, and smart biomaterials (18). Thus, the ability to access membrane dynamics on relevant length and time scales is pivotal to understanding the dynamic cooperativity taking place in lipid-protein complexes.

Here, we explore the dynamic response of model membranes to large conformational changes in associated peptides – i.e., on the time scales of protein conformations and collective membrane fluctuations. Specifically, we use the pH-low insertion peptide (pHLIP), which assumes either a surface associated (SA) or a transmembrane (TM) state, depending on the pH of the medium. At neutral pH, pHLIP adsorbs to the membrane interface, but under acidic conditions it adopts a TM α-helix conformation (21, 22). This change is driven by pHLIP's acidic groups whose protonation triggers membrane insertion (23). Notably, this pH-responsiveness imparts to pHLIP the ability to target aggressive solid tumors, typically marked by an acidic extracellular medium (24).

To probe changes in membrane dynamics associated with pHLIP's conformational changes, we used high-resolution neutron spin-echo (NSE) spectroscopy and molecular dynamics (MD) simulations. NSE results showed that TM-pHLIP results in a slowdown in the rate of membrane thickness fluctuations These observations were confirmed by coarse-grained MD simulations (25). Moreover, complementary all-atom MD simulations provided molecular-level insights into the interactions of TM-pHLIP with the membrane lipids, showing that TM-pHLIP alters lipid chain conformations and increases membrane viscosity. These findings may help us to gain insights not only into biological membrane function, but also in the design of artificial cells with tunable protein conformations.

Materials and Methods

Reagents. 1,2-dioleoyl-*sn*-glycero-3-phosphocholine (DOPC), 1,2-dioleoyl-*sn*-glycero-3-phospho-L-serine (sodium salt) (DOPS), 1,2-dimyristoyl-sn-glycero-3-phosphocholine (DMPC), and cholesterol from ovine wool (Chol) were purchased from Avanti Polar Lipids (Alabaster, AL). D_2O (99.96% D) was purchased from Cambridge Isotope Laboratories (Andover, MA). pHLIP (sequence: N_t-AAEQNPIYWARYADWLFTTPLLLLDLALLVDADEGT-C_t) was synthesized using standard protocols (P3 Biosystems, Louisville, KY) and purified to greater than 95% purity by reverse-phase high performance liquid chromatography (HPLC). Dimethyl sulfoxide (DMSO) was purchased from Fisher Scientific (Hampton, NH). Sodium phosphate dibasic (>98.5%) and sodium phosphate monobasic monohydrate (98%) were purchased from Sigma-Aldrich (St. Louis, MO) and were used to prepare sodium phosphate buffer. Sodium deuteroxide (NaOD) and deuterium chloride (DCl) were purchased from Sigma-Aldrich (St. Louis, MO) and were used to

adjust the final pH of the samples measured by neutron and x-ray scattering. Perdeuterated DOPC-d_{66} and Chol-d_{40} were synthesized as described elsewhere (26, 27).

Sample preparation. DOPC:DOPS:Chol mixtures were prepared in chloroform at a molar ratio of 76:4:20, and were consequently dried under a steady flow of argon into thin films. The films were then kept under vacuum at 45 °C for 8 hrs to 10 hrs, after which they were hydrated with a 10 mM sodium phosphate (NaP_i) pH 8.0 buffer. The lipid solution was freeze-thawed 5 times with intermittent vortex-spinning and was then extruded through a polycarbonate membrane (100 nm pore size) using a Mini Extruder (Avanti Polar Lipids, Inc., Alabaster, AL) to form large unilamellar vesicles (LUV). Samples containing pHLIP were prepared at a total lipid:peptide molar ratio of 150:1. This ratio includes any pHLIP molecules that might not be associated to the membrane. The required amount of pHLIP was introduced, in lyophilized form, into extruded vesicle suspensions at pH 8 and vortex mixed until fully incorporated. The sample pH was then changed to pH 4 to trigger the TM insertion of pHLIP. For NSE experiments, however, studies at pH 4 required a different sample prep to avoid the flocculation of membrane-unassociated pHLIP at the high vesicle concentration required in NSE measurements. In that case, pHLIP was co-dissolved with lipids in a chloroform-ethanol solution, prior to sample drying and vesicle extrusion.

Circular Dichroism. pHLIP was incubated with lipid vesicles (prepared as described earlier) in 10 mM NaP_i pH 8.0 buffer for 1 h. Afterwards, the pH was adjusted with 100 mM NaOAc or NaP_i (62.5 µL) to the desired final pH values. The final pH of the samples was measured after spectra were recorded. CD spectra were acquired using a Jasco (Easton, MD) J-815 spectropolarimeter interfaced with a Peltier system. Spectra were recorded at 25°C using a 2 mm cuvette with a scan rate of 100 nm/min and 20 to 40 accumulations. Raw data were converted into mean residue ellipticity according to: $[\theta] = \frac{\theta}{10lc(N-1)}$, where θ is the measured ellipticity, *l* is the path length of the cell in cm, *c* is the protein concentration in M, and *N* is the number of amino acids. Appropriate blanks were subtracted in all cases.

Tryptophan Fluorescence Spectroscopy. To perform a pH insertion titration, sample pH was adjusted by mixing aliquots of 100 mM stocks of sodium acetate (NaOAc), MES [2-(*N*-morpholino) ethanesulfonic acid)], or HEPES [(4-(2-hydroxyethyl)-1-piperazineethanesulfonic acid)] buffers (25 µL), to obtain the desired pH values. Final sample pH was measured using a 2.5 mm bulb pH-electrode (Microelectrodes, Inc., Bedford, NH). Tryptophan fluorescence emission spectra were recorded using a Photon Technology International (Edison, NJ) Quanta Master fluorometer at an excitation wavelength of 280 nm, an emission wavelength range of 310 nm to 400 nm, and a 3-nm excitation and emission slit setting. Lipid blanks were subtracted in all cases. Data were analyzed by monitoring changes in the fluorescence intensity (FI) at 335 nm, which is directly proportional to the population of molecular species present (28). FI pH-titrations were then fitted to determine the pK_{FI} using: $Signal = (F_a + F_b\, 10^{m(pH-pK_{FI})})/(1 + 10^{m(pH-pK_{FI})})$, where F_a is the acidic baseline, F_b is the basic baseline, *m* is the slope of the transition, and pK_{FI} is the FI midpoint of the curve, and signal is fluorescence changes.

Neutron Spin Echo (NSE) Spectroscopy. Suspensions of 100 nm diameter LUVs of DOPC:DOPS:Chol membranes were prepared in D_2O buffer at a concentration of 50 mg/mL. Bending and thickness fluctuation measurements were performed on protiated and perdeuterated (prepared with DOPC-d66 and Chol-d40) membranes , respectively. For optimal signal-to-noise, protiated and perdeuterated samples were loaded in quartz cells with path lengths of 2 mm and 4 mm, respectively. To access the different states of pHLIP, measurements were performed at two pH values, pH 8 for the surface-associated state and pH 4 for the TM state, adjusted using DCl or NaOD. Lyophilized pHLIP was weighed and added to samples at pH 8 at a lipid:peptide molar ratio of 150:1.

NSE experiments were conducted at the NIST Center for Neutron Research (NCNR) and at the Spallation Neutron Source (SNS) at Oak Ridge National Lab (ORNL). For experiments conducted on the NIST-NSE spectrometer, reduction and processing of the raw data were performed using the Data Analysis and Visualization Environment (DAVE) software (29). The data processing yields the normalized intermediate scattering function $S(q,t)/S(q,0)$ as a function of Fourier time, *t*, for discrete *q*-values within the accessed *q*-range. For lipid membranes, the decay of the intermediate scattering function is fitted to a stretched exponential function with a stretching exponent of 2/3 such that:

$$\frac{S(q,t)}{S(q,0)} = exp\left[-(\Gamma(q).t)^{\frac{2}{3}}\right], \qquad \text{(Eq. 1)}$$

where $\Gamma(q)$ represents the decay rate at individual *q*-values (see Fig. S3A), *t* is the Fourier time, and *q* is the wavevector transfer given by the neutron wavelength, λ, and scattering angle, θ, as: $q = 4\pi \sin(\theta)/\lambda$.. Experiments carried out at the SNS-NSE spectrometer covered a q-range of 0.05 Å^{-1} to 0.15 Å^{-1} for both protiated and perdeuterated membranes (albeit with different *λ* and *q* configurations). Instrument resolution and the D_2O buffer were measured under the same sample configurations for proper data reduction and normalization. Data reduction was performed using a Python script (developed at SNS) which generates the $S(q,t)/S(q,0)$ data sets required for the characterization of membrane dynamics. Subsequent data fitting and analysis were performed following the same protocols described below.

Bending fluctuation measurements on protiated membranes were analyzed using the Zilman-Granek theory for bending relaxations (30) with refinements by Watson and Brown (31) and Nagao et al (32). Accordingly, membrane relaxation rates measured on protiated membranes were solely attributed to bending relaxations, expressed as:

$$\Gamma(q) = \Gamma_{\text{bend}}(q) = 0.0069\frac{k_{\text{B}}T}{\eta_{\text{D2O}}}\sqrt{\frac{k_{\text{B}}T}{\kappa}}q^3 \qquad \text{(Eq. 2)}$$

where *κ* is the membrane bending modulus, k_B is the Boltzmann constant, T is the temperature, and η_{D2O} is the viscosity of the D_2O-buffer. In this treatment, the location of the neutral surface is assumed to be at the hydrophobic-hydrophilic interface (32).

For NSE measurements performed using *chain-perdeuterated* membrane analogs (DOPC-d_{66} and Chol-d_{40}), those were characterized by excess dynamics in addition to the q^3 signal for bending fluctuations, as demonstrated in previous work (25, 32-34). These excess dynamics are well described by the second term in Eq. 3, such that the overall relaxation rate can be expressed as:

(Eq. 3)

$$\Gamma(q) = \Gamma_{bend}(q) + \frac{q^3}{q_0^3}\frac{\Gamma_{TF}}{1+(q-q_0)^2\zeta^2},$$

where Γ_{bend} is the decay rate of bending fluctuations obtained from protiated membrane analogues, Γ_{TF} is the relaxation rate of membrane thickness fluctuations, q_0 is the peak position of the Lorentzian at which thickness fluctuation dynamics are most pronounced, and $1/\zeta$ is the half width at half maximum (HWHM) determined by the thickness fluctuation amplitude, Δd_m, such that $\zeta \approx 2D_C/(q_0.\Delta d_m)$ where $2D_C$ is the bilayer hydrocarbon thickness.

Here we note that the fits of the thickness fluctuations signals yield two physical parameters, Δd_m and Γ_{TF}, corresponding to the average fluctuation amplitude and average fluctuation rate, respectively. Given the interplay of these physical parameters with membrane biophysical parameters such as, area compressibility modulus and viscosity, a modified theoretical expression can be used to fit the thickness fluctuations signal, such that (32):

$$\frac{\Gamma}{q^3} = \frac{\Gamma_{bend}}{q^3} + \frac{K_A k_B T}{\mu q_0^3 k_B T + 4\mu q_0 K_A A_L (q - q_0)^2}, \qquad \text{(Eq. 4)}$$

where K_A is the area compressibility modulus determined from bending rigidity measurements of protiated membranes, $k_B T$ is the thermal energyA_L is the area per lipid obtained from SANS/SAXS measurements, and μ is the membrane viscosity – which is the only fit parameter for the thickness fluctuations signal.

Coarse-Grained Molecular Dynamics (CG-MD) Simulations. The coarse-grained model used in this work is based on the solvent-free approach developed by Cooke *et al* (35), where each lipid molecule is represented by three beads connected by two FENE bonds, a "head" bead representing the lipid headgroup and two "tail" beads representing the lipid hydrocarbon region. The interactions between the beads are modeled by an attractive term for tail-tail interactions and a purely repulsive term of the Weeks-Chandler-Andersen (WCA) form for head-head and head-tail interactions as described in earlier work (25). The width of the tail-tail potential-well was set to w_c =1.6 σ (where σ is the diameter of a tail bead) to achieve a membrane bending rigidity of 23.4 k_BT. The simulations were performed using an initial vesicle configuration consisting of N = 18996 lipid molecules preassembled with an approximate radius of 30 σ and an area per lipid of ~ 1 σ^2 for both the inner and outer leaflets. For lipid vesicles containing transmembrane peptides, 300 rods composed of 8 connected beads were included within the membrane. The stiffness of the rods was maintained through an angle potential with a bending rigidity of 64 k_BT, which results in an approximate rod persistence length of 62 σ. The transmembrane configuration of the rods within the membrane was obtained by assigning repulsive interactions between the first and last beads of the rod and the tail beads of lipid molecules. The remaining rod-beads experienced attractive interactions with those of the lipid tails, similar to those of tail-tail lipid interactions. To avoid rod aggregation, a repulsive potential was assigned to all bead-bead interactions within the rod. This model was demonstrated in previous studies to accurately capture NSE signals for membrane bending and thickness fluctuations (25). In this work, we adapt the same model to illustrate the effect of pHLIP insertion on membrane thickness fluctuations.

Simulated NSE data were produced as follows: The static scattering function, $S(q)$, of simulated vesicles was calculated from the density−density correlation function by taking the discrete Fourier transform of the density distribution of all lipid beads, such that $S(q) = 1/N \langle \rho_{\vec{q}} \rho_{-\vec{q}} \rangle$. Membrane fluctuation signals were calculated from simulations as $S(q,t)/S(q,0) = 1/N \langle \rho_{\vec{q}}(\Delta t) \rho_{-\vec{q}} \rangle$, which represents the time autocorrelation of the scattering function, $S(q)$, after an elapsed time Δt. This is analogous to the intermediate dynamic scattering function measured by NSE. Analysis of the temporal decays in $S(q,t)/S(q,0)$, following the procedure developed in a previous work (25), yielded the relaxation rates of membrane thickness fluctuations.

Atomistic MD Simulations. All systems were prepared using the CHARMM-GUI web server (36). Coordinates for pHLIP (GGEQNPIYWARYADWLFTTPLLLLDLALLVDADEGT) were obtained from the X-ray crystal structure of bacteriorhodopsin (PDB 1FBB) using residues 72 to 107. The Q105E mutation was carried out to be consistent with the composition of pHLIP, and all acidic residues (E3, D14, D25, D31, D33, E34) were protonated. pHLIP was inserted as a

transmembrane α-helix into a lipid membrane with the same compositions described above, i.e., DOPC:DOPS:Chol at 76:4:20 mole fraction. The simulations were set up with 50 waters per lipid and 100 mM NaCl, via the replacement method. All systems were equilibrated for 50 ns with a 2 fs timestep in NAMD 2.13 (37) in the *NPT* ensemble (T = 310 K and P = 1 atm), using the Langevin thermostat (38) and Nosé-Hoover barostat (39). For equilibration, the charmm36 force field for lipids (40) and proteins (41) and the TIP3P model for water (42) were used, with standard cutoffs applied (10 Å switching and 12 Å cutoff) for non-bonded forces. For production runs, the coordinates of the last frame of the equilibration trajectory were converted to be consistent with AMBER force field topology (ff14SB (43), lipid17 (44), and OPC for water (45)). A small minimization and equilibration of 1 ns was performed, with a 2 fs timestep in the *NPT* ensemble (T = 310 K and P = 1 atm) using the Monte-carlo barostat with semi-anisotropic pressure coupling to preserve the aspect ratio of lateral plane of the bilayer and the Langevin thermostat. Minimization and equilibration were performed employing the sander MD engine in AMBER18 (46), with a cutoff for non-bonded forces of 8 Å. Production runs were carried out with the GPU-accelerated version of pmemd in AMBER18 using the same configurations as minimization and equilibration. Ten simulations per system were conducted with an aggregate time of 10 μs each. Analysis was performed using a combination of VMD (47), cpptraj in AmberTools (46), LOOS (48) and in-house scripts. Snapshots of trajectories were rendered in VMD, and plots were generated with gnuplot (49), respectively.

Small-Angle X-ray and Neutron Scattering (SAXS/SANS): D_2O suspensions of 100-nm diameter extruded vesicles composed of DOPC, DOPS, and Chol (as well as their perdeuterated variants DOPC-d_{66} and Chol-d_{40}) were prepared at ~ 20 mg/mL. To access the two states of pHLIP, measurements were performed at two pH values, pH 8 for surface-associated pHLIP and pH 4 for TM pHLIP, obtained by using either NaOD or DCl, respectively. Lyophilized pHLIP was weighed and added to vesicle suspensions (pH 8) at a lipid:peptide ratio of 150:1. For TM pHLIP measurements, the peptide was co-dissolved with lipids and cholesterol in a chloroform-ethanol solution to ensure its full integration in the membranes and avoid peptide aggregation in solution when the pH was changed from 8 to 4. After drying the solution into thin films, the same extrusion process, as described above, was used to extrude the pHLIP-containing membranes into 100 nm diameter vesicles.

Scattering data were analyzed following data analysis protocols outlined by Doktorova et al (50). Differently contrasted scattering data (i.e., SANS data for different deuterated lipid variants, and SAXS data) were jointly refined with a model that accounts for coherent scattering contributions from transverse scattering length density (SLD) variations within the bilayer. Transverse SLD profiles probed by SANS and SAXS determined the nuclear and electronic composition, respectively, of the lipid headgroup and hydrocarbon regions in the lipid bilayers. For protein-membrane complexes, the SLD profile is, in principle, influenced by the presence of surface-bound or inserted protein. However, due to the low mass fraction of protein used in these experiments (< 1%), we neglected the protein contribution to the SLD profile. Thus, any detectable changes in the scattering curves are due to the effect of the protein on the lipid bilayer structure. The transverse SLD profiles were derived from the underlying lipid volume probability distributions within the bilayer, modeled as the sum of separate distributions for the lipid headgroups and hydrocarbon chains. The total unit cell volume was calculated as a mole-fraction weighted sum of lipid volumes obtained from literature (Table S1) and constrained in the fit, leaving as adjustable parameters the area per lipid A_L and headgroup thickness, D_H. Additional structural parameters, including the total bilayer thickness D_B and the hydrocarbon thickness, $2D_C$, were derived from relationships between the adjustable parameters and the lipid headgroup and hydrocarbon

volumes. From the unit cell volume probability profile, neutron SLD and electron density (ED) profiles were then obtained as a sum of the separate headgroup and hydrocarbon volume probability distributions multiplied by their respective total scattering lengths (Table S1).

For each nominal sample composition (e.g., molar ratio of DOPC:DOPS:Chol is 76:4:20) SANS samples were prepared with two different contrasts using protiated and perdeuterated variants of DOPC (i.e., DOPC or DOPC-d_{66}) and Chol (i.e., Chol or Chol-d_{40}, Fig. S9). Joint analysis of all available SANS and SAXS data for a given sample composition and pH was implemented in Mathematica 11.0 (Wolfram Research, Champaign, IL). Uncertainties in structural parameters were obtained from a bootstrap method (51). Briefly, a synthetic scattering data set consistent with experimental noise was generated as follows:

$$I_{syn}(q) = I_{fit}(q) + X(q),$$
$$X(q) \sim N\left[0, \sigma_{exp}(q)\right]. \quad \text{(Eq. 5)}$$

In the previous equations, I_{fit} is the best-fit intensity value and X, which represents noise, is a random variable drawn from a Gaussian distribution whose standard deviation corresponds to the experimentally determined uncertainty, σ_{exp}. Synthetic data sets for X-ray and neutron data were jointly analyzed as previously described to determine the structural parameters $A_{L,syn}$, $D_{B,syn}$, $2D_{C,syn}$, and $D_{HH,syn}$. This process was repeated 100 times to generate populations of synthetic structural parameters; the uncertainties reported in Table S1 are the standard deviations of these populations.

Complementary SANS data analysis was performed using the core-multi-shell model in the SasView software, specifically a three-shell vesicle model (head-tail-head) (52). The model assumes a Gaussian distribution of the vesicle radius (fitted over the low-q range of the data) but does not consider gradients in the interfaces between the headgroup and hydrocarbon layers (due to the Gaussian distribution of different lipid subgroups). The results of this analysis are presented in Table S1 and are compared to the more refined approach described above.

Results

Previous biophysical studies on pHLIP have largely focused on understanding how the membrane influences pHLIP cancer treatment efficacy (53-55). As previously demonstrated, pHLIP adsorbs to the membrane surface at neutral pH but inserts into the membrane under acidic conditions (21). Here, we studied the effect of pHLIP on membrane dynamics and structure. Measurements were performed at room temperature (25 ºC) on lipid vesicles composed of a 76:4:20 molar mixture of 1,2-dioleoyl-*sn*-3 glycero-3-phosphocholine (DOPC), 1,2-dioleoyl-*sn*-glycero-3-phosphoserine (DOPS), and cholesterol (Chol) (56) at a lipid:peptide (L:P) molar ratio of 150:1. The anionic lipid DOPS was used to ensure vesicle unilamellarity (57, 58), as shown in Fig. S1. This choice of membrane composition was motivated by earlier studies reporting optimal pHLIP insertion in DOPC membranes with 20 mol% Chol (59).

Using circular dichroism measurements, we showed that at pH 8 pHLIP adsorbs to the vesicle surface in a largely unstructured conformation (Fig. S2) (60), but it inserts into the membrane when the pH is dropped to pH 4 where pHLIP transforms in to a TM helix (23, 61). The membrane insertion of pHLIP is characterized by its p*K*, which depends on lipid composition (62-64). For instance, the presence of the negatively charged lipid phosphatidylserine (PS) decreases the membrane insertion p*K* (62, 64) as does the presence of cholesterol (65). Here, we observed that

the inclusion of both PS and Chol in PC membranes decreases pHLIP's p*K* to its lowest value yet observed for the peptide, *i.e.*, p*K* = 4.90 ± 0.08 (Fig. S2), suggesting that the membrane's chemical properties have an additive effect on the p*K* of insertion.

Bending fluctuations are controlled by the mechanical properties of the membrane, typically described by the bending rigidity modulus, and have been studied extensively both experimentally and theoretically (66, 67). On the other hand, fluctuations around the average membrane thickness have been less explored despite being linked to several vital membrane phenomena, including ion channel gating (68, 69) and hydrophobic mismatch (refs?). Unlike other spectroscopy methods, NSE can simultaneously access the length (a few nm) and timescales (~ 100 ns) over which membrane thickness fluctuations occur (68, 70, 71). Fig. S3A shows typical NSE intermediate scattering functions, $S(q,t)/S(q,0)$, as described above. Fits of the intermediate scattering functions using the elastic-sheet fluctuation model $S(q,t)/S(q,0) = exp\left[-(\Gamma(q).t)^{2/3}\right]$, yielded the relaxation rates, Γ(*q*), of bending and/or thickness fluctuations at different *q*-values (or inverse length scales) (30). Plots of Γ(*q*) for *protiated* vesicles in deuterated buffer showed the typical q^3-dependence (Fig. S3B, blue data points) of membrane bending fluctuations (30). Fitting the data to the model described in Eq. 2 yielded the membrane bending modulus, *κ*. We observed that pHLIP did not cause substantial changes to *κ*, neither in its SA (pH 8) nor TM (pH 4) states, as all *κ* values were within experimental error (Table 1 and Fig. S4).

Table 1. Dynamic membrane parameters obtained from the analysis of NSE and all-atom MD simulations. Error bars represent ± 1 standard deviation.

		Bending Fluctuations			**Thickness Fluctuations**		**Diff. const.**
pH	pHLIP	κ [a] (k_BT)	K_A [b] (N/m)	Γ_{TF} [c] (10^{-3} ns^{-1})	Δd_m [d] (Å)	μ [e] (nPa.s.m)	D [f] (10^{-5} cm^2/s)
8	--	30.3 ± 2.5	0.26 ± 0.02	7.3 ± 0.9	3.5 ± 0.6	31.9 ± 3.5	
4	--	29.2 ± 1.3	0.26 ± 0.02	7.3 ± 1.7	3.4 ± 0.8	32.0 ± 4.1	1.28 ± 0.72
8	+	26.9 ± 1.8	0.23 ± 0.02	6.5 ± 2.3	3.4 ± 1.0	30.5 ± 3.5	
4	+	32.9 ± 2.7	0.28 ± 0.03	1.7 ± 0.6	3.8 ± 1.5	105.9 ± 54.8	0.59 ± 0.06

NSE parameters: [a] bending rigidity modulus obtained from measurements on protiated membranes with the bending rigidity modulus as the only fit parameter (see Eq. 2); [b] area compressibility modulus calculated by the polymer-brush model, $K_A = 24\kappa/(2D_C)^2$ using the experimentally measured κ values; [c] relaxation rate of membrane thickness fluctuations obtained on chain-perdeuterated membranes following Eq. 3; [d] amplitude of membrane thickness fluctuations, calculated as $\Delta d_m \approx 2D_C/\zeta q_0$, using the mechanical thickness, $2D_C$, as well as q_0 and ζ corresponding to the peak-position and width of the Lorentzian distribution describing the excess dynamics due to thickness fluctuations (see the NSE section for more details);; and [e] membrane viscosity obtained from analysis of the membrane thickness fluctuations using Eq. 4. [f] Diffusion constant calculated from mean-square displacements in all-atom MD simulations.

In contrast to results from protiated membranes, NSE measurements of *chain-perdeuterated* membrane analogs (i.e., DOPC-d_{66} and Chol-d_{40}) showed a clear deviation from the q^3 dependence in the relaxation rates at q ~ 0.08 Å^{-1}, a value which corresponds to the membrane thickness (Fig. S3B). The observed excess dynamics are associated with membrane thickness

fluctuations (32-34) and were analyzed using Eq. 3 (Fig. S3, red data points). Analysis of these signals (Fig. 1) yielded key physical descriptors of membrane thickness fluctuations, namely the fluctuation rate, Γ_{TF}, and the fluctuation amplitude, Δd_m (Fig. 1A and Table 1). The results revealed that TM-pHLIP induced a four-fold decrease in Γ_{TF}, but SA-pHLIP had little impact on Γ_{TF}. Control experiments of lipid-only samples showed that variations in pH had no effect on either κ (72) or membrane thickness fluctuations (Fig. S5 and Table 1). Interestingly, no changes to Δd_m were observed in either conformation of pHLIP (Fig. S6 and Table 1). The data, therefore, imply that the suppression of thickness fluctuations due to TM-pHLIP is the result of a slowdown in the thickness fluctuation rate, and not the result of a decrease in the thickness fluctuation amplitude.

Our NSE conclusions were supported by coarse-grained molecular dynamics (CG-MD) simulations of membrane fluctuations. CG-MD were performed on large unilamellar lipid vesicles with and without transmembrane peptide-like inclusions resembling TM-pHLIP (Fig. S7). As seen in Fig. 1B, the simulated vesicle with TM peptides of the same hydrophobic thickness as the membrane showed a noticeable suppression in the membrane thickness fluctuation signal, relative to the lipid-only vesicle. Analysis of the simulation results (Figure 1B and Table S2) corroborated the conclusions from NSE experiments, indicating that the presence of a transmembrane helix decreases the rate of membrane thickness fluctuations but not the fluctuation amplitude.

To relate membrane thickness fluctuations to other biophysical membrane properties, we used the polymer-brush model that we modified according to previous studies (56, 73). This analysis describes the area compressibility modulus as $K_A = \varsigma\kappa/(2D_C)^2$ (74), where ς is a constant that defines the degree of coupling between the two bilayer leaflets (75) (herein set to ς = 24) and $2D_C$ is the mechanical thickness of the membrane. In the q-range where thickness fluctuations dominate, the relaxation rates are dictated by the membrane viscosity, μ, such that $\Gamma_{TF} \approx K_A/\mu$ (76-78). Put together, this yields a modified expression (Eq. 3) that enables direct determination of μ (see Eq. 4). Based on this, the minimal changes in the measured bending rigidities (Fig. S4) indicate that neither SA- nor TM-pHLIP alter K_A (Table 1 and Fig. S8). Further, the constant thickness fluctuation rate, Γ_{TF}, obtained with SA-pHLIP indicates that the surface association of the peptide does not affect μ – in striking contrast to TM-pHLIP which caused a large increase in μ (Fig. 1C and Table 1).

To understand the molecular mechanism by which TM-pHLIP modulates membrane thickness fluctuations and viscosity, we used all-atom MD simulations. We first determined the effect of pHLIP on lipid dynamics, as measured by the mean square displacement (MSD) of the DOPC headgroups and then used the MSD data to calculate the lipid diffusion constant. Doing this, we observed that TM-pHLIP strongly decreased lipid mobility (Fig. 2 and Table 1), as it is expected for a more viscous membrane. MSD analysis included both in-plane lipid diffusion and lipid movement along the membrane normal. The average MSD in the direction normal to the membrane plane had similar values in the absence (20.3 × 10^3 Å^{-2}/ps) and presence (20.8 × 10^3 Å^{-2}/ps) of TM-pHLIP. This observation indicates that the effect of pHLIP on lipid mobility is limited to in-plane motions and supports the NSE and CG-MD results, implying that pHLIP does not alter the amplitude of membrane thickness fluctuations (Table S2).

These observations were further validated by small-angle X-ray and neutron scattering (SAXS/SANS) on membranes with SA- and TM-pHLIP. With SANS, we used deuterium labeling to maximize the neutron contrast between the protiated lipid headgroups and deuterated acyl chains of the membrane (79). Joint analysis of the SANS and SAXS data (80-82) resulted in membrane structure, including membrane thickness, D_B, and area per lipid, A_L. Our results indicate that the addition of pHLIP does not alter D_B, A_L, or the average membrane hydrophobic thickness (Table S1, Fig. S9-12), in agreement with measurements made by all-atom MD simulations (Fig. S13). These observations are also in agreement with a previous pHLIP study

using 1-palmitoyl-2-oleoyl-*sn*-glycero-3-phosphocholine (POPC) membranes (83) in which neither pHLIP adsorption nor insertion were found to alter membrane structure – even at elevated peptide concentrations. Based on recently measured scaling relationships (84), the negligible effect of pHLIP on A_{L} supports the NSE conclusion that K_A is not affected by the different states of pHLIP (Table 1), further adding to the evidence that the decrease in the rate of thickness fluctuations ($\Gamma_{TF} \approx K_A/\mu$) induced by TM-pHLIP is due to increased membrane viscosity.

In fluid membranes, acyl chain dynamics allow for the interaction between the lipid's acyl chain terminal methyl group (CH_3) and the polar headgroups – a phenomenon known that has been referred to as lipid snorkeling (85, 86). We hypothesized that if TM-pHLIP indeed promoted lipid tails to experience dynamic excursions into the headgroup region, this would lead to increased molecular friction within the bilayer, causing an increase in membrane viscosity and an observable slowdown of thickness fluctuations. To investigate acyl chain dynamics, we measured the distance between the C_α of the lipid headgroup and the terminal CH_3 group from atomistic MD simulations in the presence of TM-pHLIP (Fig. 3). In the absence of pHLIP, we observed that, as expected, most CH_3 groups were located at the bilayer midplane, approximately 21 Å from the headgroup (Fig. 3A, black line) (85). However, in the presence of TM-pHLIP, the distance distribution changed, and new features appeared at shorter distances, indicating that acyl chains close to pHLIP explored the headgroup region more frequently. For the lipid molecules found within a 15 Å radius of pHLIP, we observed two discrete acyl chains populations with CH_3-C_α distances of ~ 11 Å and ~ 15 Å, and a reduction of extended acyl chains (~ 21 Å) (Fig. 3A *top*, inset). These results suggest that in pHLIP's vicinity, lipid acyl chains snorkel with increased frequency (Fig. 3C). However, for lipids 15-25 Å away from pHLIP, their CH_3-C_α distance is similar to the peptide-free membranes. This result indicates pHLIP's influence on lipid dynamic excursions is limited to lipids in its vicinity (2-3 lipid shells around TM-pHLIP).

Discussion

Experiment and simulation indicated that TM-pHLIP suppressed the rate of membrane thickness fluctuations, Γ_{TF} (Fig. 1 A-B), in membranes with no hydrophobic mismatch and resulted in an "effective" increase in membrane viscosity, μ. On the other hand, SA-pHLIP did not affect either Γ_{TF} or μ (Fig. 1 and Table 1), indicating that changes to these two parameters are specific to the interaction of TM-pHLIP with the lipid acyl chains. It is important to point out that although the increase in μ is fully supported by our analysis of the NSE data, its magnitude requires further assessment. Specifically, our analysis of thickness fluctuations assumed that the two bilayer leaflets are coupled according to the polymer-brush model and that the transition of pHLIP to its TM state does not change the interleaflet coupling. In the polymer brush model, the two bilayer leaflets are loosely coupled with a coupling constant ς = 24 that is proportional to the coupling strength between the leaflets. However, variations in the coupling constant have been previously observed (87, 88). If we consider this possibility and assume an extreme coupling scenario in which TM-pHLIP causes the two leaflets to be fully coupled (i.e., ς = 12), this would still result in a two-fold increase in membrane viscosity relative to pHLIP-free membranes. Assuming that the membrane viscosity and diffusion constant are inversely proportional, this would suggest that TM-pHLIP causes an approximate 2-fold decrease in the diffusion constant, in close agreement with the MSD results from all-atom MD simulations. Although one would expect an intermediate value for the bilayer leaflet coupling constant, a more accurate estimate of this parameter would require additional experimental studies that are beyond the scope of this work.

A feature of fluid bilayers that is often overlooked is the fact that their acyl chain terminal methyl groups snorkel to the membrane surface and interact with the lipid headgroups. For example, 2D NMR studies of different composition lipid bilayers have shown that the terminal

methyl groups of lipid fatty acid chains interact with the choline headgroups (85). This effect was also observed in our atomistic MD simulations, which show a smooth distribution of CH_3-C_α distances with a long tail at low values (black line, Fig. 3A). In comparison, simulations with TM-pHLIP showed a shift in the distribution to smaller distances indicating longer residence times of the CH_3 groups near the lipid headgroups (see supplementary Video). More importantly, our probability distribution contained peaks at ~11 Å and ~15 Å, indicating a statistical increase in the number of acyl chains that explore the lipid headgroup region (red line, Fig. 3A *top*). The acyl chain snorkeling of lipids may facilitate the intermolecular proximity between the tail methyl groups and choline headgroups. This result indicates that for lipids in the vicinity of pHLIP, their terminal methyl groups snorkel to the lipid-water interface at an increased frequency. As a result, this would increase the free space available to nearby lipids, allowing their chains to explore a larger conformational space. Based on these findings, we propose that the increased frequency in acyl chain snorkeling results in higher in-plane friction due to increased acyl chain entanglement, in a way that is analogous to irregularly-shaped epithelial cells exhibiting reduced 2D mobility (89). Additionally, lipid tails from the opposite monolayer can fill the space left by a snorkeled tail, increasing interleaflet coupling (90, 91). Any combination of these two effects would cause an apparent increase in membrane viscosity, which can result in a dampening of the thickness fluctuation rate.

Supporting Material. Supporting Information is provided for supplementary results, details of data analysis, and additional figures.

Author Contributions. H.L.S., B.M., F.A.H, R.A., and F.N.B designed the research. H.L.S., F. A. H., and R.A. performed SANS and NSE experiments and analyzed data. V.B.C. and B.M. designed and performed atomistic MD simulations. J.M.C. and B.G.S. designed and performed coarse-grained MD simulations. W.Q. collected and analyzed NMR data. A.C.D. assisted with anisotropy measurements. J.K. assisted with SANS/SAXS data analysis. L.S. assisted with NSE data collection and analysis. R.F.S. synthesized deuterated lipids. H.L.S., R.A., F.A.H., J.K., and F.N.B. wrote the manuscript.

Acknowledgements. The authors thank Dr. Michihiro Nagao, Dr. Elizabeth G. Kelley, and Dr. Piotr Zolnierczuk for technical assistance and useful discussions of NSE experiments. We thank Vanessa P. Nguyen and Justin M. Westerfield for comments on the manuscript. This work was partially supported by grant R35GM140846 from the NIH (F.N.B.), NSF grant No. MCB-1817929 (F.A.H.), NSF grant No. MCB-2137154 (R.A.), and by funds from the UT-ORNL Joint Institute for Biological Sciences (JIBS) to F.N.B. Support was also received from the UTK-ORNL Science Alliance in the form of a Joint Directed Research and Development Award (to F.N.B.). W.Q. was supported by NIH grant R01GM125853 and SUNY Binghamton. J.K. was supported through the Scientific User Facilities Division of the Department of Energy (DOE) Office of Science, sponsored by the Basic Energy Science (BES) Program, DOE Office of Science, under Contract No. DEAC05-00OR22725. Sample preparation and characterization were supported by the Biophysical Characterization Laboratory suite of the Shull Wollan Center at ORNL. Access to the NG3-30m SANS and NGA-NSE was provided by the Center for High Resolution Neutron Scattering, a partnership between the National Institute of Standards and Technology and the National Science Foundation under agreement no. DMR-1508249. Research conducted at ORNL's Spallation Neutron Source was sponsored by the Scientific User Facilities Division, Office of Basic Energy Sciences, US Department of Energy. Oak Ridge National Laboratory is managed by UT-Battelle, LLC under US DOE Contract No. DE-AC05-00OR22725. The coarse-grained molecular dynamics simulations and associated computational research were supported by the Center for Nanophase Materials Sciences, a US DOE Office of Science User Facility at Oak Ridge National Laboratory. This study used resources of the Oak Ridge Leadership Computing Facility at Oak Ridge National Laboratory.

Note. Any mention of commercial products is for information only; it does not imply recommendation or endorsement by NIST.

References.

1. R. Phillips, T. Ursell, P. Wiggins, P. Sens, Emerging roles for lipids in shaping membrane-protein function. *Nature* **459**, 379-385 (2009).
2. M. Ø. Jensen, O. G. Mouritsen, Lipids do influence protein function—the hydrophobic matching hypothesis revisited. *Biochimica et Biophysica Acta (BBA) - Biomembranes* **1666**, 205-226 (2004).
3. E. Perozo, A. Kloda, D. M. Cortes, B. Martinac, Physical principles underlying the transduction of bilayer deformation forces during mechanosensitive channel gating. *Nature Structural Biology* **9**, 696-703 (2002).
4. M. F. Brown, Soft Matter in Lipid–Protein Interactions. *Annual Review of Biophysics* **46**, 379-410 (2017).
5. I. Levental, E. Lyman, Regulation of membrane protein structure and function by their lipid nano-environment. *Nature Reviews Molecular Cell Biology* 10.1038/s41580-022-00524-4 (2022).
6. S. I. Sukharev, W. J. Sigurdson, C. Kung, F. Sachs, Energetic and spatial parameters for gating of the bacterial large conductance mechanosensitive channel, MscL. *J Gen Physiol* **113**, 525-540 (1999).
7. T. Ursell, K. C. Huang, E. Peterson, R. Phillips, Cooperative Gating and Spatial Organization of Membrane Proteins through Elastic Interactions. *PLOS Computational Biology* **3**, e81 (2007).
8. M. F. Brown, Modulation of rhodopsin function by properties of the membrane bilayer. *Chem Phys Lipids* **73**, 159-180 (1994).
9. C. Hidalgo, D. D. Thomas, N. Ikemoto, Effect of the lipid environment on protein motion and enzymatic activity of sarcoplasmic reticulum calcium ATPase. *Journal of Biological Chemistry* **253**, 6879-6887 (1978).
10. O. S. Andersen, R. E. Koeppe, 2nd, Bilayer thickness and membrane protein function: an energetic perspective. *Annu Rev Biophys Biomol Struct* **36**, 107-130 (2007).
11. E. Lindahl, M. S. P. Sansom, Membrane proteins: molecular dynamics simulations. *Current Opinion in Structural Biology* **18**, 425-431 (2008).
12. J. A. Lundbaek, S. A. Collingwood, H. I. Ingólfsson, R. Kapoor, O. S. Andersen, Lipid bilayer regulation of membrane protein function: gramicidin channels as molecular force probes. *J R Soc Interface* **7**, 373-395 (2010).
13. T.-H. Lee, V. Hofferek, F. Separovic, G. E. Reid, M.-I. Aguilar, The role of bacterial lipid diversity and membrane properties in modulating antimicrobial peptide activity and drug resistance. *Current Opinion in Chemical Biology* **52**, 85-92 (2019).
14. Y. Jaillais, T. Ott, The Nanoscale Organization of the Plasma Membrane and Its Importance in Signaling: A Proteolipid Perspective1 [OPEN]. *Plant Physiology* **182**, 1682-1696 (2019).
15. B. Lillemeier, C. Klammt, How membrane structures control T cell signaling. *Frontiers in Immunology* **3** (2012).
16. W. Cho, R. V. Stahelin, Membrane-Protein Interactions in Cell Signaling and Membrane Trafficking. *Annual Review of Biophysics and Biomolecular Structure* **34**, 119-151 (2005).
17. K. Henzler-Wildman, D. Kern, Dynamic personalities of proteins. *Nature* **450**, 964-972 (2007).
18. J.-H. Ha, S. N. Loh, Protein Conformational Switches: From Nature to Design. *Chemistry – A European Journal* **18**, 7984-7999 (2012).

19. B. J. Grant, A. A. Gorfe, J. A. McCammon, Large conformational changes in proteins: signaling and other functions. *Current Opinion in Structural Biology* **20**, 142-147 (2010).
20. L. M. P. Chataigner, N. Leloup, B. J. C. Janssen, Structural Perspectives on Extracellular Recognition and Conformational Changes of Several Type-I Transmembrane Receptors. *Frontiers in Molecular Biosciences* **7** (2020).
21. Y. K. Reshetnyak, M. Segala, O. A. Andreev, D. M. Engelman, A monomeric membrane peptide that lives in three worlds: in solution, attached to, and inserted across lipid bilayers. *Biophys J* **93**, 2363-2372 (2007).
22. J. C. Deacon, D. M. Engelman, F. N. Barrera, Targeting acidity in diseased tissues: mechanism and applications of the membrane-inserting peptide, pHLIP. *Arch Biochem Biophys* **565**, 40-48 (2015).
23. H. L. Scott, J. M. Westerfield, F. N. Barrera, Determination of the Membrane Translocation pK of the pH-Low Insertion Peptide. *Biophys J* **113**, 869-879 (2017).
24. V. Estrella *et al.*, Acidity generated by the tumor microenvironment drives local invasion. *Cancer Res* **73**, 1524-1535 (2013).
25. J. Y. Carrillo, J. Katsaras, B. G. Sumpter, R. Ashkar, A Computational Approach for Modeling Neutron Scattering Data from Lipid Bilayers. *J Chem Theory Comput* **13**, 916-925 (2017).
26. J. D. Nickels *et al.*, Mechanical Properties of Nanoscopic Lipid Domains. *J Am Chem Soc* **137**, 15772-15780 (2015).
27. S. Chakraborty *et al.*, How cholesterol stiffens unsaturated lipid membranes. *Proceedings of the National Academy of Sciences* 10.1073/pnas.2004807117, 202004807 (2020).
28. A. S. Ladokhin, S. Jayasinghe, S. H. White, How to Measure and Analyze Tryptophan Fluorescence in Membranes Properly, and Why Bother? *Analytical Biochemistry* **285**, 235-245 (2000).
29. R. T. Azuah *et al.*, DAVE: A Comprehensive Software Suite for the Reduction, Visualization, and Analysis of Low Energy Neutron Spectroscopic Data. *Journal of Research of the National Institute of Standards and Technology* **114**, 341-358 (2009).
30. A. G. Zilman, R. Granek, Undulations and Dynamic Structure Factor of Membranes. *Physical Review Letters* **77**, 4788-4791 (1996).
31. M. C. Watson, F. L. Brown, Interpreting membrane scattering experiments at the mesoscale: the contribution of dissipation within the bilayer. *Biophys J* **98**, L9-L11 (2010).
32. M. Nagao, E. G. Kelley, R. Ashkar, R. Bradbury, P. D. Butler, Probing Elastic and Viscous Properties of Phospholipid Bilayers Using Neutron Spin Echo Spectroscopy. *J Phys Chem Lett* **8**, 4679-4684 (2017).
33. A. C. Woodka, P. D. Butler, L. Porcar, B. Farago, M. Nagao, Lipid bilayers and membrane dynamics: insight into thickness fluctuations. *Phys Rev Lett* **109**, 058102 (2012).
34. R. Ashkar *et al.*, Tuning membrane thickness fluctuations in model lipid bilayers. *Biophys J* **109**, 106-112 (2015).
35. I. R. Cooke, K. Kremer, M. Deserno, Tunable generic model for fluid bilayer membranes. *Phys Rev E Stat Nonlin Soft Matter Phys* **72**, 011506 (2005).
36. S. Jo, T. Kim, V. G. Iyer, W. Im, CHARMM-GUI: a web-based graphical user interface for CHARMM. *J Comput Chem* **29**, 1859-1865 (2008).
37. J. C. Phillips *et al.*, Scalable molecular dynamics with NAMD. *J Comput Chem* **26**, 1781-1802 (2005).
38. R. L. Davidchack, R. Handel, M. V. Tretyakov, Langevin thermostat for rigid body dynamics. *The Journal of Chemical Physics* **130**, 234101 (2009).
39. H. A. Posch, W. G. Hoover, F. J. Vesely, Canonical dynamics of the Nosé oscillator: Stability, order, and chaos. *Phys Rev A Gen Phys* **33**, 4253-4265 (1986).
40. J. B. Klauda *et al.*, Update of the CHARMM All-Atom Additive Force Field for Lipids: Validation on Six Lipid Types. *The Journal of Physical Chemistry B* **114**, 7830-7843 (2010).

41. R. B. Best *et al.*, Optimization of the additive CHARMM all-atom protein force field targeting improved sampling of the backbone ϕ, ψ and side-chain χ(1) and χ(2) dihedral angles. *Journal of chemical theory and computation* **8**, 3257-3273 (2012).
42. W. L. Jorgensen, J. Chandrasekhar, J. D. Madura, R. W. Impey, M. L. Klein, Comparison of simple potential functions for simulating liquid water. *The Journal of Chemical Physics* **79**, 926-935 (1983).
43. J. A. Maier *et al.*, ff14SB: Improving the Accuracy of Protein Side Chain and Backbone Parameters from ff99SB. *Journal of Chemical Theory and Computation* **11**, 3696-3713 (2015).
44. I. R. Gould, Skjevik A.A., C. J. Dickson, B. D. Madej, R. C. Walker, Lipid17: A Comprehensive AMBER Force Field for the Simulation of Zwitterionic and Anionic Lipids. *in prep* (2018).
45. S. Izadi, R. Anandakrishnan, A. V. Onufriev, Building Water Models: A Different Approach. *The Journal of Physical Chemistry Letters* **5**, 3863-3871 (2014).
46. D. e. a. Case, Amber18. *University of California, San Francisco.* (2019).
47. W. Humphrey, A. Dalke, K. Schulten, VMD - Visual Molecular Dynamics. *J. Molec. Graphics.* **14**, 33-38 (1996).
48. T. D. Romo, N. Leioatts, A. Grossfield, Lightweight object oriented structure analysis: Tools for building tools to analyze molecular dynamics simulations. *Journal of Computational Chemistry* **35**, 2305-2318 (2014).
49. T. Williams, C. Kelley, Gnuplot 4.5: an interactive plotting program. . (2011).
50. M. Doktorova *et al.*, Preparation of asymmetric phospholipid vesicles for use as cell membrane models. *Nat Protoc* **13**, 2086-2101 (2018).
51. W. H. Press, S. A. Teukolsky, W. T. Vetterling, B. P. Flannery, *Numerical Recipes in C: The Art of Scientific Computing* (Cambridge Univeristy Press, ed. 2, 1992).
52. e. a. M. Doucet, SasView Version 4.1.2.
53. O. A. Andreev *et al.*, Mechanism and uses of a membrane peptide that targets tumors and other acidic tissues in vivo. *Proc Natl Acad Sci U S A* **104**, 7893-7898 (2007).
54. O. A. Andreev, D. M. Engelman, Y. K. Reshetnyak, pH-sensitive membrane peptides (pHLIPs) as a novel class of delivery agents. *Mol Membr Biol* **27**, 341-352 (2010).
55. C. J. Cheng *et al.*, MicroRNA silencing for cancer therapy targeted to the tumour microenvironment. *Nature* **518**, 107-110 (2015).
56. S. Chakraborty *et al.*, How cholesterol stiffens unsaturated lipid membranes. *Proceedings of the National Academy of Sciences* **117**, 21896-21905 (2020).
57. N. Kucerka, J. Pencer, J. N. Sachs, J. F. Nagle, J. Katsaras, Curvature effect on the structure of phospholipid bilayers. *Langmuir* **23**, 1292-1299 (2007).
58. H. L. Scott *et al.*, On the Mechanism of Bilayer Separation by Extrusion, or Why Your LUVs Are Not Really Unilamellar. *Biophysical Journal* **117**, 1381-1386 (2019).
59. F. N. Barrera, J. Fendos, D. M. Engelman, Membrane physical properties influence transmembrane helix formation. *Proceedings of the National Academy of Sciences* **109**, 14422-14427 (2012).
60. F. N. Barrera *et al.*, Roles of carboxyl groups in the transmembrane insertion of peptides. *J Mol Biol* **413**, 359-371 (2011).
61. H. L. Scott *et al.*, The negative charge of the membrane has opposite effects on the membrane entry and exit of pH-low insertion peptide. *Biochemistry* **54**, 1709-1712 (2015).
62. A. Kyrychenko, V. Vasquez-Montes, M. B. Ulmschneider, A. S. Ladokhin, Lipid headgroups modulate membrane insertion of pHLIP peptide. *Biophys J* **108**, 791-794 (2015).
63. H. L. Scott, F. A. Heberle, J. Katsaras, F. N. Barrera, Phosphatidylserine Asymmetry Promotes the Membrane Insertion of a Transmembrane Helix. *Biophysical Journal* **116**, 1495-1506 (2019).
64. H. L. Scott *et al.*, The Negative Charge of the Membrane Has Opposite Effects on the Membrane Entry and Exit of pH-Low Insertion Peptide. *Biochemistry* **54**, 1709-1712 (2015).

65. F. N. Barrera, J. Fendos, D. M. Engelman, Membrane physical properties influence transmembrane helix formation. *Proc Natl Acad Sci U S A* **109**, 14422-14427 (2012).
66. P. Bassereau, B. Sorre, A. Lévy, Bending lipid membranes: Experiments after W. Helfrich's model. *Advances in Colloid and Interface Science* **208**, 47-57 (2014).
67. W. Helfrich (1973) Elastic Properties of Lipid Bilayers: Theory and Possible Experiments. in *Zeitschrift für Naturforschung C*, p 693.
68. M. Nagao, Observation of local thickness fluctuations in surfactant membranes using neutron spin echo. *Phys Rev E Stat Nonlin Soft Matter Phys* **80**, 031606 (2009).
69. L. Movileanu, D. Popescu, S. Ion, A. I. Popescu, Transbilayer Pores Induced by Thickness Fluctuations. *Bulletin of Mathematical Biology* **68**, 1231-1255 (2006).
70. F. Mezei, Neutron spin echo: A new concept in polarized thermal neutron techniques. *Zeitschrift für Physik A Hadrons and nuclei* **255**, 146-160 (1972).
71. R. Ashkar *et al.*, Neutron scattering in the biological sciences: progress and prospects. *Acta Crystallographica Section D* **74**, 1129-1168 (2018).
72. M. B. Boggara, A. Faraone, R. Krishnamoorti, Effect of pH and Ibuprofen on the Phospholipid Bilayer Bending Modulus. *The Journal of Physical Chemistry B* **114**, 8061-8066 (2010).
73. M. Doktorova, M. V. LeVine, G. Khelashvili, H. Weinstein, A New Computational Method for Membrane Compressibility: Bilayer Mechanical Thickness Revisited. *Biophysical Journal* **116**, 487-502 (2019).
74. D. Boal, *Mechanics of the Cell* (Cambridge University Press, Cambridge, ed. 2, 2012), DOI: 10.1017/CBO9781139022217.
75. W. Rawicz, K. C. Olbrich, T. McIntosh, D. Needham, E. Evans, Effect of chain length and unsaturation on elasticity of lipid bilayers. *Biophys J* **79**, 328-339 (2000).
76. R. J. Bingham, S. W. Smye, P. D. Olmsted, Dynamics of an asymmetric bilayer lipid membrane in a viscous solvent. *EPL (Europhysics Letters)* **111** (2015).
77. U. Seifert, S. A. Langer, Viscous Modes of Fluid Bilayer Membranes. *Europhysics Letters (EPL)* **23**, 71-76 (1993).
78. E. G. Kelley, P. D. Butler, M. Nagao, "Collective Dynamics in Model Biological Membranes Measured By Neutron Spin Echo Spectroscopy" in Characterization of Biological Membranes (Walter de Gruyter, Inc. , Boston, MA, 2019), chap. 4, pp. 131-176.
79. O. G. Mouritsen, M. Bloom, Mattress model of lipid-protein interactions in membranes. *Biophysical journal* **46**, 141-153 (1984).
80. F. A. Heberle *et al.*, Model-based approaches for the determination of lipid bilayer structure from small-angle neutron and X-ray scattering data. *Eur Biophys J* **41**, 875-890 (2012).
81. N. Kucerka *et al.*, Lipid bilayer structure determined by the simultaneous analysis of neutron and X-ray scattering data. *Biophys J* **95**, 2356-2367 (2008).
82. N. Kucerka, M. P. Nieh, J. Katsaras, Fluid phase lipid areas and bilayer thicknesses of commonly used phosphatidylcholines as a function of temperature. *Biochim Biophys Acta* **1808**, 2761-2771 (2011).
83. T. Narayanan *et al.*, pHLIP Peptide Interaction with a Membrane Monitored by SAXS. *J Phys Chem B* **120**, 11484-11491 (2016).
84. E. G. Kelley, P. D. Butler, R. Ashkar, R. Bradbury, M. Nagao, Scaling relationships for the elastic moduli and viscosity of mixed lipid membranes. *Proceedings of the National Academy of Sciences* **117**, 23365-23373 (2020).
85. M. Mihailescu *et al.*, Acyl-chain methyl distributions of liquid-ordered and -disordered membranes. *Biophys J* **100**, 1455-1462 (2011).

86. D. Huster, K. Arnold, K. Gawrisch, Investigation of Lipid Organization in Biological Membranes by Two-Dimensional Nuclear Overhauser Enhancement Spectroscopy. *The Journal of Physical Chemistry B* **103**, 243-251 (1999).
87. P. Shchelokovskyy, S. Tristram-Nagle, R. Dimova, Effect of the HIV-1 fusion peptide on the mechanical properties and leaflet coupling of lipid bilayers. *New J Phys* **13**, 25004-25004 (2011).
88. H. Usuda *et al.*, Interleaflet coupling of n-alkane incorporated bilayers. *Physical Chemistry Chemical Physics* 10.1039/C9CP06059F (2020).
89. J.-A. Park *et al.*, Unjamming and cell shape in the asthmatic airway epithelium. *Nature Materials* **14**, 1040 (2015).
90. J. Wong-Ekkabut *et al.*, Effect of lipid peroxidation on the properties of lipid bilayers: a molecular dynamics study. *Biophys J* **93**, 4225-4236 (2007).
91. H. S. Muddana, R. R. Gullapalli, E. Manias, P. J. Butler, Atomistic simulation of lipid and DiI dynamics in membrane bilayers under tension. *Phys Chem Chem Phys* **13**, 1368-1378 (2011).

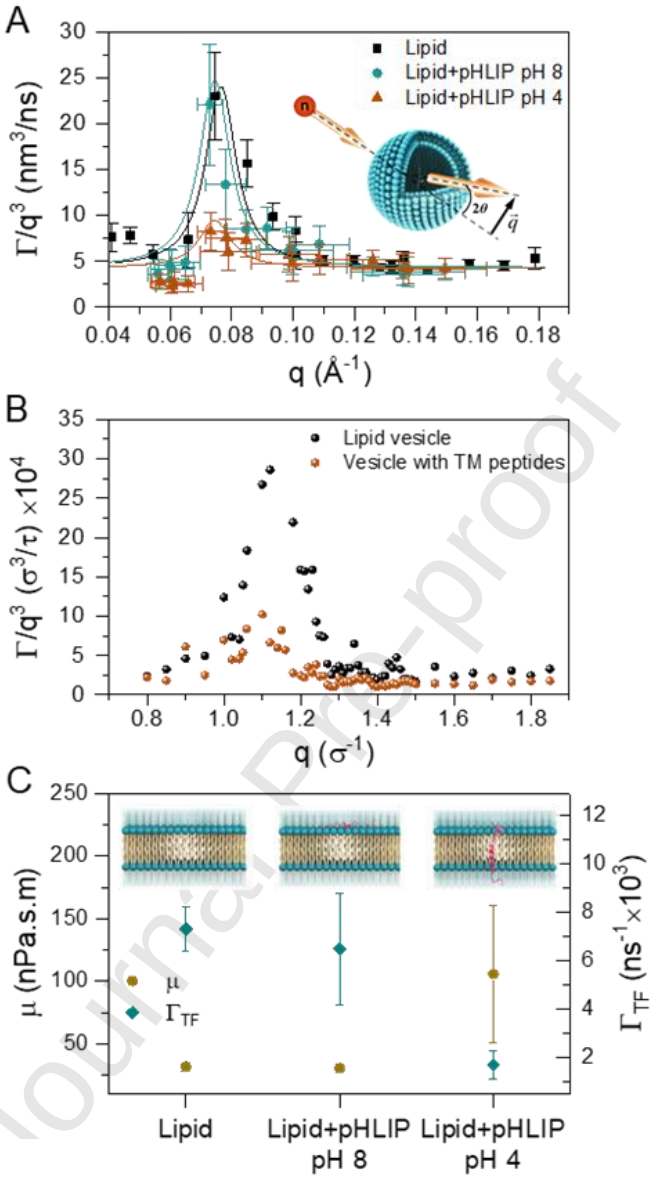

Figure 1. (A) NSE data showing the normalized relaxation rate, Γ/q^3, as a function of q for tail perdeuterated membranes. Data are shown in the absence (black) and presence of pHLIP in its SA (blue, pH 8) and TM (red, pH 4) states. Lines are fits to the data using Eq. D. Inset shows an NSE schematic where lipid vesicles scatter neutrons with a scattering angle 2θ and wavevector transfer $\vec{q}$. (B) CG-MD simulation of membrane fluctuation signals as detected by NSE, for vesicles without (black) and with (red) TM peptide incorporated. (C) The rates of thickness fluctuations show remarkable suppression in the presence of TM pHLIP and no changes with SA pHLIP. Membrane viscosity changes exhibit a similar trend, as only TM pHLIP increases viscosity. Error bars represent ± 1 S.D. Experiments were performed at a 150:1 lipid to peptide molar ratio.

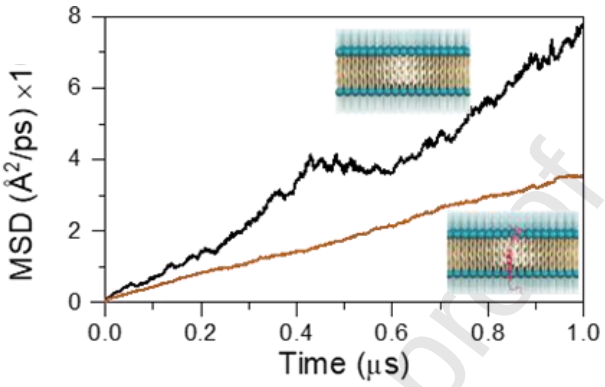

Figure 2. Atomistic MD simulations show a decrease in the mean-squared displacement (MSD) of the lipid headgroups in the presence of TM-pHLIP (red) compared to lipid-only membranes (black).

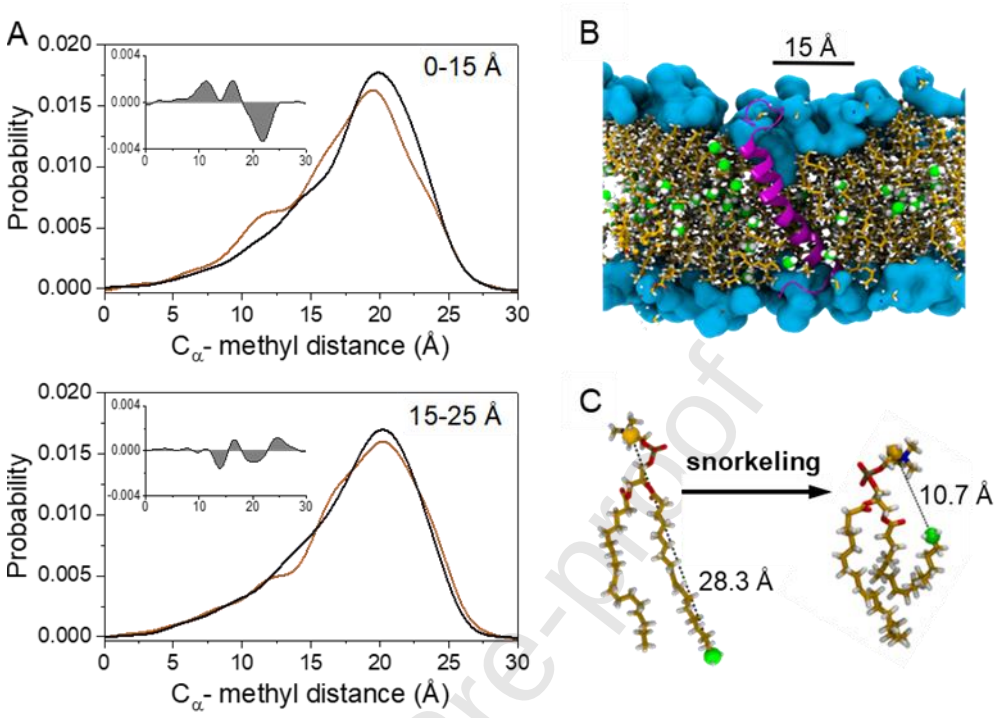

Figure 3. (A) Probability distribution of the distance between the CH_3 groups of DOPC oleoyl chains and the plane formed by the Cα of the choline headgroups. Black lines show data from neat bilayers, and red lines consider only lipids within 15 Å of pHLIP (top), or between 15 and 25 Å from the helix (bottom). Insets show the subtraction between red and black lines. (B) Representative snapshots of a DOPC/DOPS/Chol bilayer containing TM pHLIP. Phospholipid headgroups are shown in blue, and tails in yellow. CH_3 groups are shown as green spheres. Cholesterol molecules are shown in a ball and stick representation. (C) A representative DOPC molecule with fully extended acyl chains can snorkel reducing the distance to the choline headgroup in the presence of TM-pHLIP. C_α (yellow) and CH_3 (green) are shown as spheres and are used for distance measurements.

Declaration of interests

☒ The authors declare that they have no known competing financial interests or personal relationships that could have appeared to influence the work reported in this paper.

☐ The authors declare the following financial interests/personal relationships which may be considered as potential competing interests:

Graphical abstract

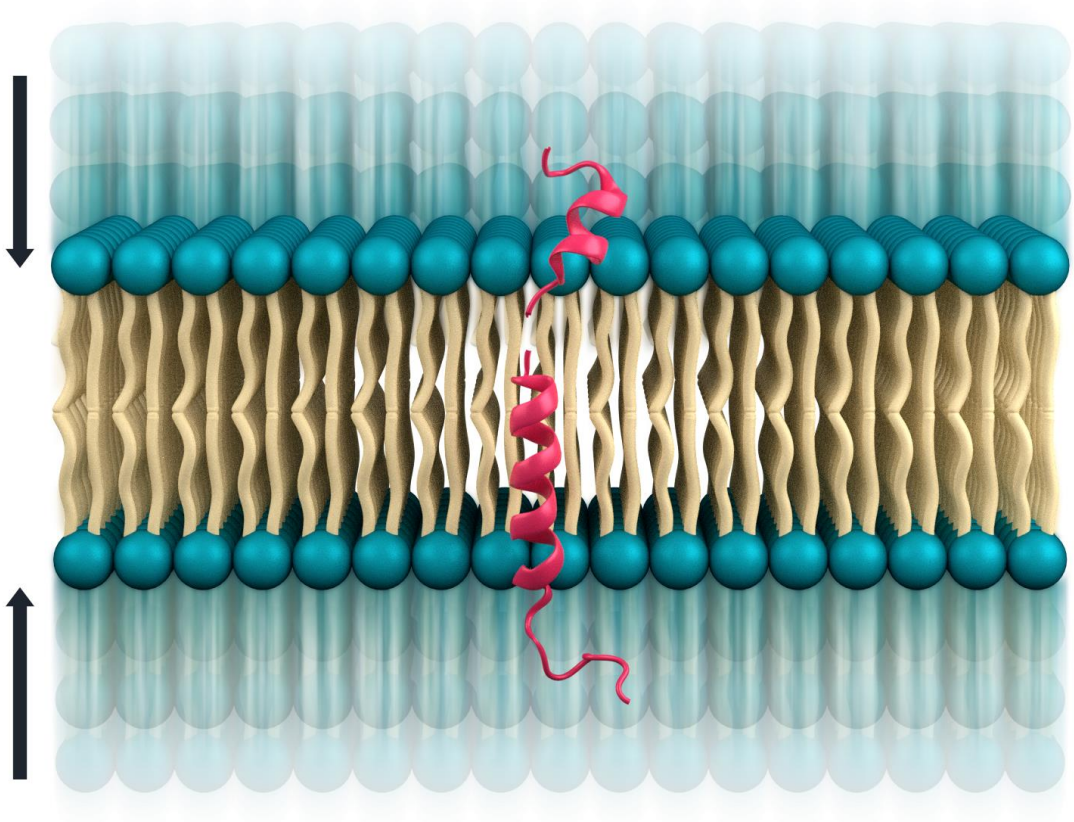

Highlights

- Neutron spin echo reveals that when the pHLIP peptide adopts a transmembrane helix conformation, it reduces the rate at which membrane thickness fluctuates.
- Transmembrane pHLIP also increases membrane viscosity.
- Molecular dynamics simulation reveals kinking of lipid acyl chains around the helix, which could explain the increased viscosity.
- The effects of pHLIP are conformation-dependent, as no changes are observed when pHLIP binds to the membrane surface at neutral pH.